scientific reports

Check for updates

OPEN

Shape optimisation of rim structure of aluminium alloy car wheels based on 90° impact test

Guangdong Zhang[1]✉, Shike Tao[1], Yangyang Zhou[2], Zhen Ye[2], Jianjun Lu[2], Risheng Li[2], Shihui Li[2], Linzhen Zhou[1] & Tong Deng[3]

Automotive wheels are critical components for vehicular safety, with the rim subjected primarily to radial bending loads during operation. Balancing rim thickness and structural integrity under these loading conditions is imperative. This paper develops and validates an innovative shape optimisation approach utilising the 90° wheel impact test methodology. A simplified 2D finite element model was formulated for rim optimisation to address the computational inefficiency of conventional 3D simulation-based optimisation in product development while exploiting rim geometry's rotational symmetry. The design of experiments technique was employed to identify key stiffness-influencing factors and their interactions. Subsequent shape optimisation, guided by analytical insights, yielded an engineered rim configuration. Comparative 3D simulations of 90° impact performance demonstrated a 0.51 mm reduction in inner rim flange deformation alongside a 59 g mass reduction, achieving dual objectives of enhanced structural performance and lightweighting. This streamlined optimisation methodology significantly enhances development efficiency while providing engineers with critical insights into parametric influences on rim strength characteristics.

Keywords Rim, Design of experiments, Shape optimisation, 90° impact simulation

The lightweight design of vehicles helps to reduce energy consumption and carbon emissions[1]. For spinning components such as wheels, the energy loss due to increased mass is 1.5 times that of non-rotating components[2]. Therefore, any weight control of the wheel is favourable for energy saving and carbon emission reduction for vehicles.

Currently, the primary approaches of wheel lightweight design include: (1) the extensive use of lightweight materials, such as aluminium alloy[2,3], glass fibre[4,5], magnesium alloy[6], and carbon fibre[7]; (2) innovative assembled wheel designs, such as magnesium-aluminium alloy assembled wheels[8,9] and lightweight alloy assembled wheels using multiple connection methods[10] (e.g., riveting and adhesive bonding); (3) biomimetic designs of wheel structures[11]. The manufacturing of fibre material wheels and magnesium alloy wheels presents challenges, and the costs are relatively high[12,13], which limits their applications and is only suitable for racing cars or supercars. Modular wheel technology requires further development and has yet to be widely promoted. There is limited research on biomimetic wheels, and production and processing challenges remain. As a lightweight material, aluminium alloy materials are aesthetically pleasing[14] and have several advantages, such as good corrosion resistance, formability, and recyclability[15], and effectively balance lightweight and cost requirements, making them widely used for vehicle wheels.

Although lightweight wheels enhance vehicular dynamic response characteristics[16], the design process encounters significant challenges. This involves reconciling mass reduction objectives[17] with compliance to critical safety protocols encompassing dynamic bending fatigue resistance, radial fatigue endurance, and impact resilience specifications. Of these performance criteria, structural crashworthiness assumes particular importance in impact-load-bearing configurations[18], mandating comprehensive validation through standardised impact testing methodologies to verify operational integrity under transient loading conditions.

As one of the wheel impact tests, the 90° impact test assesses wheel strength against perpendicular impacts during driving according to the QC/T 991-2015 standard[19], which encounters road pits or frontal stone impacts. During the test, the wheel rim primarily withstands radial bending loads. The wheel's performance is evaluated by measuring the deformation of the inner rim flange of the wheel or the cracking range of the wheel

[1]School of Mechanical Engineering, Yancheng Institute of Technology, Yancheng 224051, Jiangsu, China. [2]Hebei High Strength and Toughness Lightweight Wheel Technology Innovation Centre, Baoding Lizhong Wheel Manufacturing Co., Ltd., Baoding 071000, Hebei, China. [3]The Wolfson Centre for Bulk Solids Handling Technology, Faculty of Engineering and Science, University of Greenwich, London ME4 4TB, UK. ✉email: gdzhang@ycit.edu.cn

circumference at the rim after the test. Optimising rim structure is beneficial for enhancing the strength of the rim. However, traditional rim optimisation mainly depends on engineers' experience by increasing the angle of the rim groove bottom or adding the local thickness of the rim[20] and then evaluating wheel strength through simulations or tests. Experience-based optimisation methods exhibit certain limits. For example, increasing rim thickness will result in greater wheel weight, which affects heat dissipation[21] and leads to the deterioration of the brake system and tyres[22]. Additionally, the wheel impact test is inherently destructive, and even the rim design needs to repeat modifications until it meets the requirements. This results in prolonged product development cycles and increased costs.

Numerical simulation has been increasingly used to replace traditional impact tests and explore lightweight design solutions for wheels[23], such as topology and shape optimisation[24,25]. Hu et al.[26] identified rim and flange thickness as design variables and conducted an optimised wheel design based on radial and bending fatigue tests, achieving a 5.42% reduction in weight. Sun et al.[27] established an optimisation model of a wheel that comprehensively considers the effects of rim stiffness, modal characteristics, and bending fatigue life, resulting in optimised structural parameters for the wheel. Wang et al.[28] used spline curves instead of straight lines and arcs to establish the rim cross-section model, implementing parametric modelling by adding dimensional constraints, and applying a multi-island genetic algorithm combined with sequential quadratic programming optimisation methods for the rim optimisation, achieving a weight reduction of 7.1%. Wang et al.[29] proposed a shape optimisation method based on the force path analysis, visualising the force transmission paths within the rim cross-section and determining the final shape through parameter optimisation methods, subsequently confirming the optimised results via simulations and tests. Yang et al. [30] investigated the effects of different rim structural dimensions on the radial fatigue stress of the inner rim flange, optimising the weak areas of the rim and verifying the optimised wheel through rig tests and field trials. These findings indicated decreased cracks in the optimised rim, significantly enhancing the wheel's lifespan.

The structural optimisation of wheel rims through numerical simulations demonstrates significant technical merits. However, the multivariate nature of rim geometrical parameters and insufficient understanding of their individual and interactive effects on structural integrity frequently led to suboptimal optimisation efficiency. This inefficiency stems from the computationally intensive 3D simulation analyses required by conventional approaches, which struggle to meet contemporary requirements for accelerated wheel development cycles. The study addresses these challenges by establishing a simplified 2D finite element model based on standardised 90° impact test protocols. Through the systematic design of experiments (DOE) methodology, the research quantitatively elucidates the influence patterns, weight coefficients, and parameter interactions governing rim structural performance. Subsequent implementation of shape optimisation led to an enhanced rim configuration that was ultimately validated through comprehensive 3D dynamic simulation analyses.

The 90° impact test and simulation

90° impact test

The experimental configuration for the 90° impact test is presented in Fig. 1. The wheel-hub assembly undergoes vertical fixation to a rigid support structure that is directly coupled to the ground foundation. Precise axial and circumferential positional adjustments ensure impact localisation between the rim centreline and inner flange region. The operational sequence comprises three distinct phases: (1) Vertical positioning of the impact hammer through elevation reduction to establish tyre proximity and enable axial coursework alignment; (2) Controlled axial displacement of the support structure to achieve concentric correspondence between the tyre cross-sectional centroid and hammer impact surface periphery; (3) Angular orientation optimisation through wheel rotation to position the designated impact zone (typically co-located with the valve stem orifice) perpendicularly beneath the impact hammer's axis of trajectory.

Following the alignment of the testing apparatus, the hammer assembly is elevated to a predetermined vertical elevation and subsequently gravity-released to impart impact loading on the wheel-tyre system. Upon impact

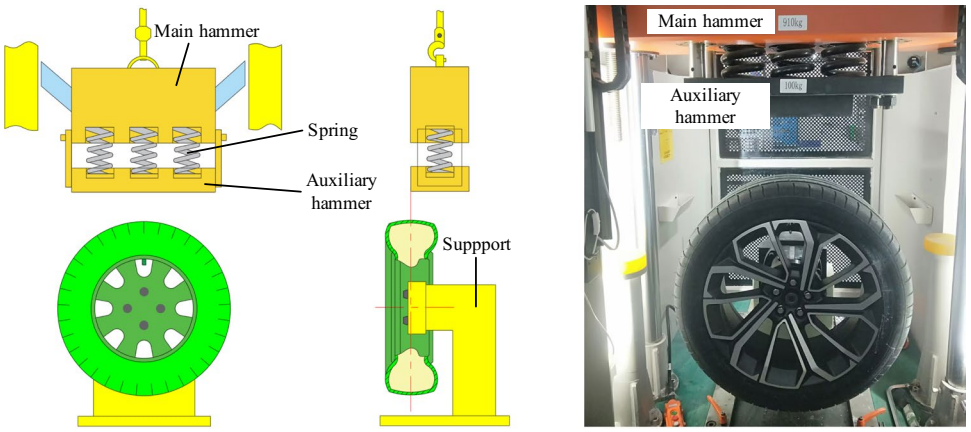

Fig. 1. The setup of the 90° impact test. (**a**) Schematic diagram of the test, (**b**) Physical image of the test.

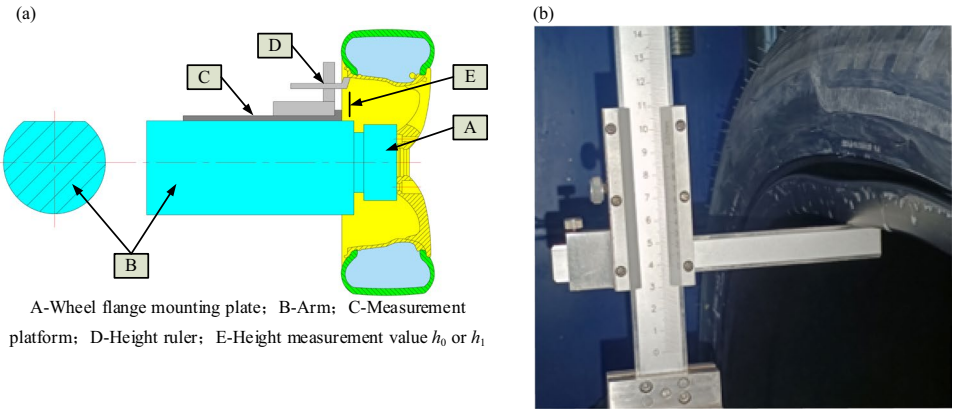

Fig. 2. The measurement of deformation. (**a**) Measurement method, (**b**) Measurement of inner rim flange deformation.

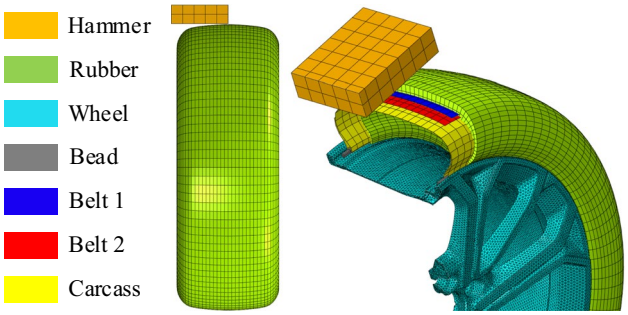

Fig. 3. FEA model of 90° impact test.

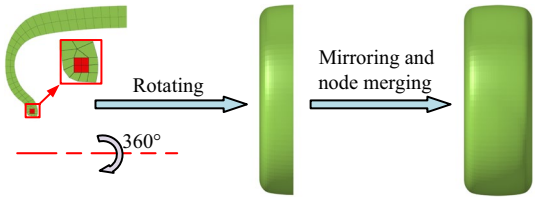

Fig. 4. Three-dimensional tyre elements.

termination, the hammer mechanism undergoes retraction from the tyre interface to facilitate elastic recovery of the rim structure. After a stabilisation period of approximately 60 s, the permanent plastic deformation of the inner rim flange is quantitatively assessed through metrological procedures illustrated in Fig. 2, with this deformation metric serving to evaluate rim strength and inform structural optimisation requirements. The QC/T 991-2015 standard defines rim deformation as the diametral dimensional differential between pre-impact and post-impact conditions at the localised impact zone.

Simulation of the 90° impact test

A mass-produced aluminium alloy wheel with nominal dimensions 20 × 9.0 J was selected for this investigation, paired with a 275/45 R20 pneumatic tyre. A 3D finite element model was developed based on the 90° impact testing specifications, as shown in Fig. 3. The initial moment of the wheel impact simulation occurs when the hammer contacts the tyre. Since the tyre needs to be inflated before the impact simulation, and tyre inflation causes tread displacement, a specific distance between the tread and the hammer has been left in advance to ensure that the tyre is fully inflated without any interference. The distance is determined through inflation simulations, yielding a value of 3.5 mm.

The wheel is discretised using 4-node tetrahedral elements[31] with a uniform element size of 5 mm. The tyre model is constructed through a sequential process involving manual discretisation of the half cross-sectional profile (including bead components), followed by rotational, mirroring, and node-merging operations to generate three-dimensional tyre elements, as illustrated in Fig. 4. Reinforcement components (belt and carcass)

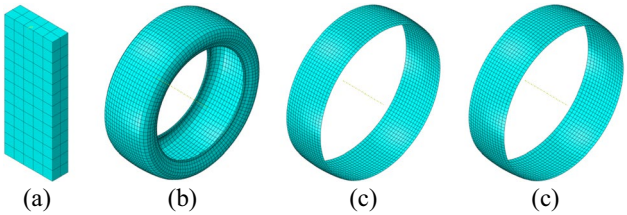

Fig. 5. Meshing results. (**a**) Hammer, (**b**) Carcass, (**c**) Belt 1#, (**d**) Belt 2#.

Material name	Young's modulus (GPa)	Poisson's ratio	Density (kg/m^3)	Section area (mm^2)	Cord spacing (mm)	Angle with the tyre meridian plane (°)
Carcass	10	0.4	1200	0.241	1	0
Belt 1	200	0.3	7800	0.141	1.176	63
Belt 2	200	0.3	7800	0.141	1.176	117

Table 1. Cord material parameters.

Material name	Density (kg/m^3)	Young's modulus (GPa)	Poisson's ratio
Wheel	2700	71	0.33
Hammer	3.5E5	210	0.3
Bead	7800	210	0.3

Table 2. Material parameters of wheel, hammer, and bead. The density of the hammer is a virtual value, which is calculated based on the mass and volume of the hammer.

are discretised with a characteristic element size of 15 mm. Given the hammer's substantially higher stiffness relative to both the tyre-wheel assembly and its mechanical irrelevance to the study's objectives, the hammer is modelled as a rigid body employing a coarser element size of 30 mm. Figure 5 presents the resulting finite element meshes for the belt reinforcement layers, carcass structure, and impact hammer assembly.

Materials

The tyre rubber exhibits a 1200 kg/m^3 density and follows the Yeoh hyperelastic material model with coefficients C_{10} = 0.771 MPa, C_{20} = – 0.386 MPa, and C_{30} = 0.197 MPa. The simulation neglects strain rate dependency effects in the rubber material[32]. The carcass and belt components, modelled as discrete layers of uniformly distributed fibre reinforcements embedded within the rubber matrix, have their respective material properties detailed in Table 1. Mechanical characteristics for the aluminium alloy wheel, impact hammer, and bead assembly are summarised in Table 2.

The tyre fulfils a critical energy-absorbing function while significantly affecting resultant rim deformation. Model calibration involves the refinement of iterative belt and carcass material parameters through multiple impact simulations to achieve tyre modelling fidelity[33].

Since the maximum impact stress exerted on the wheel during testing exceeds the yield strength of the aluminium alloy, the incorporation of hardening characteristics becomes imperative[34], demonstrating the material's post-yield mechanical behaviour. Notably, the impact zone in the 90° impact test occurs proximal to the inner rim flange, differing fundamentally from 13° impact analyses where deformation mechanisms manifest at the outer rim and spoke assemblies. Consequently, the constitutive properties of spoke components are excluded from consideration. Material specimens harvested from the inner rim flange yield the hardening curve through standard tensile testing protocols, as illustrated in Fig. 6.

Boundary conditions

In the finite element model, the structural stiffening effect induced by tyre inflation pressure is incorporated by applying 0.255 MPa uniform pressure on the inner cavity surface bounded by the tyre-rim interface. Gravitational effects are explicitly considered in the simulation. The wheel mount hub is subjected to fixed constraints reflecting its rigid connection to ground-anchored supports, with bolt preload effects omitted from the analysis as per the schematic configuration presented in Fig. 7.

The hammer is imposed by an initial velocity obtained from the theory as indicated in Eq. (1):

$$v_0 = \sqrt{2gh} \tag{1}$$

where h is the falling height of the hammer, and g is the gravity acceleration (9.8 m/s^2).

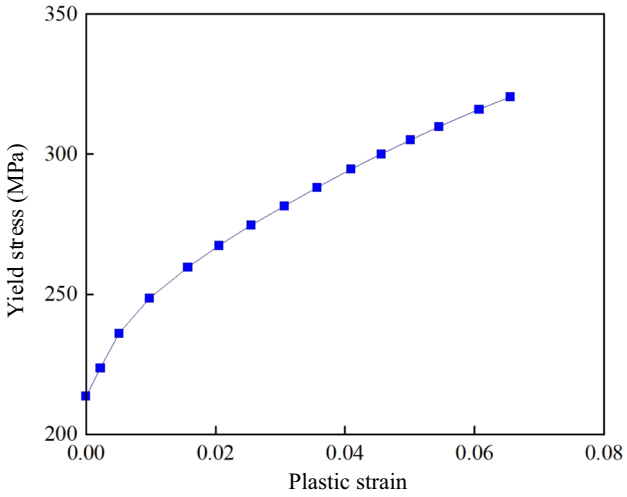

Fig. 6. Hardening characteristic of the aluminium alloy.

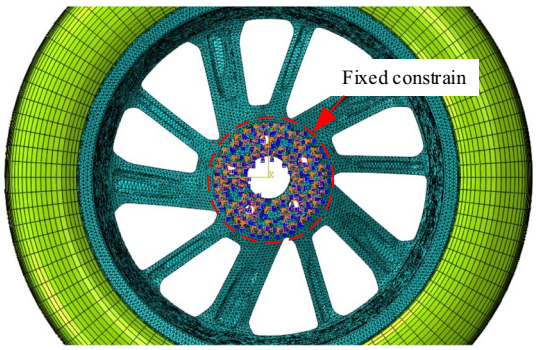

Fig. 7. The fixed constraint on the hub.

Two test and simulation sets were performed at 209 mm and 228 mm hammer drop heights, yielding initial velocities of 2024.0 mm/s and 2114.0 mm/s, respectively. A general contact algorithm was implemented given the transient impact duration, negligible frictional energy dissipation[35], and complex interfacial interactions (Fig. 8). This approach accounts for tyre self-contact during severe deformation through "Normal Hard Contact" normal behaviour and "Tangential Frictionless" tangential properties to monitor surface response characteristics.

Simulation procedure

The simulation of the 90° impact test is conducted in three steps:

(1) Inflating the tyre; (2) Assigning the initial velocity to the hammer; (3) Simulating the impact.

All steps are executed using the Abaqus/Explicit solver.

The tyre inflation was completed in 0.003 s for the first step. So, the duration of the first step is 0.003 s.

In the second step, a time interval of 1×10^{-8} s is assigned to impose the hammer with an initial velocity to neglect the falling displacement over an extremely short time.

In the third step, the impact duration is set to 0.25 s to ensure the hammer rebounds after reaching the lowest point, and the inner rim flange restores elastic deformation, allowing for the acquisition of the final plastic deformation at the impact region.

Test and simulation results

The results of the 90° impact tests and corresponding simulations are illustrated in Fig. 9 and Table 3, demonstrating a maximum relative error of 5.04%, deemed negligible in engineering contexts. These outcomes validate the precision of the finite element model and provide a robust basis for subsequent rim structural optimisation.

Optimisation of the rim structure

Rim structure optimisation aims to develop lightweight rim configurations that meet stringent strength requirements. While the rim exhibits numerous structural parameters, three-dimensional (3D) simulation-

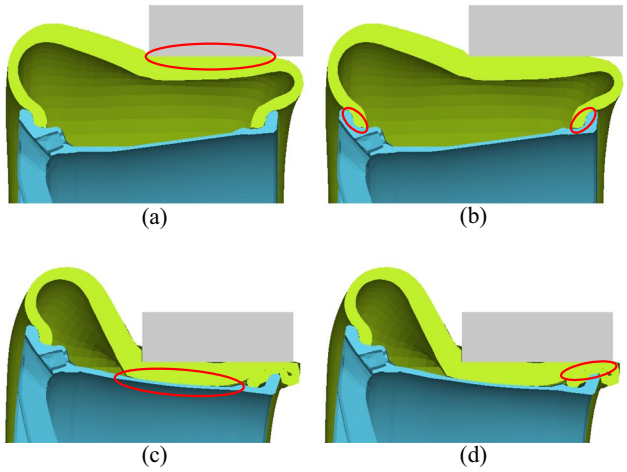

Fig. 8. Types of contact during the impact process. (**a**) The contact between tread and hammer, (**b**) The contact between bead and flange, (**c**) The contact between tyre and rim, (**d**) The self-contact of tyre.

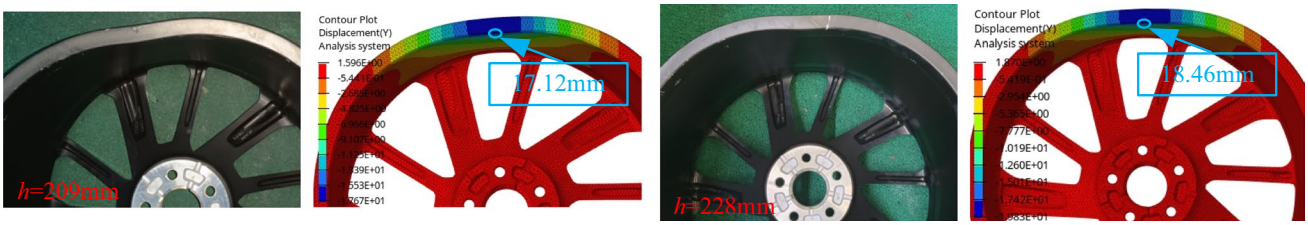

Fig. 9. Test and simulation results.

Impact height (mm)	Deformation of the inner rim flange		Relative difference (%)
	Test value (mm)	Simulation value (mm)	
209	16.32	17.12	4.90
228	19.44	18.46	5.04

Table 3. Test and simulation results.

based optimisation proves computationally intensive and inefficient, presenting significant challenges in meeting contemporary wheel development timelines.

Considering that the rim is a rotational symmetry component about the wheel axis with constant cross-sectional geometry, in addition, studies have shown that increasing the stiffness of the rim cross-section helps enhance the wheel's strength. Therefore, the rim's cross-sectional profile has been selected as the primary investigative focus. The loading scenario can be effectively represented by a radial concentrated load *F*, facilitating the development of a simplified two-dimensional finite element model for 90° impact analysis, as illustrated in Fig. 10. While the geometrical profile of rim flanges (inner and outer) and bead seats remains constrained by tyre assembly requirements, their wall thickness remains adjustable per operational specifications. Consequently, the central region of the rim cross-section has been designated as the principal optimisation domain.

The Design of Experiments (DOE) procedure was implemented via the HyperStudy software platform integrated with OptiStruct as the finite element solver. The DOE methodology was applied to investigate the primary influencing factors on rim stiffness and their interrelationships. After this analytical phase, a structural optimisation strategy for the rim was formulated based on the parametric analysis outcomes, employing the shape-optimisation capabilities inherent in OptiStruct software to execute the rim geometrical optimization.

Design of experiment

The rim structural parameters were modelled within OptiStruct software, with the Design of Experiments' (DOE) full-factorial approach being utilised to analyse their effects on mechanical stiffness and parametric interactions. This methodology enables systematic investigation of variable influence relationships on performance objectives through minimal experimental iterations[25], supported by statistical analysis techniques in post-processing stages

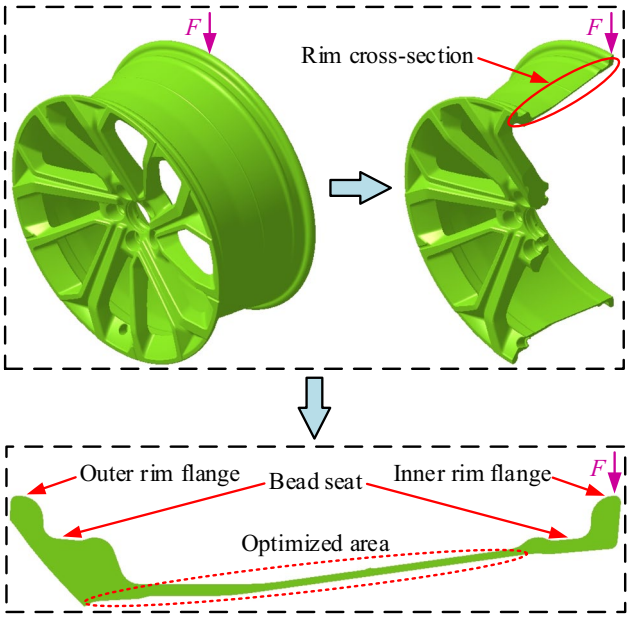

Fig. 10. A simplified two-dimensional finite element model of 90° impact.

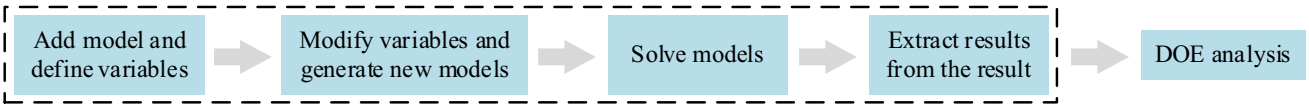

Fig. 11. The process of DOE analysis.

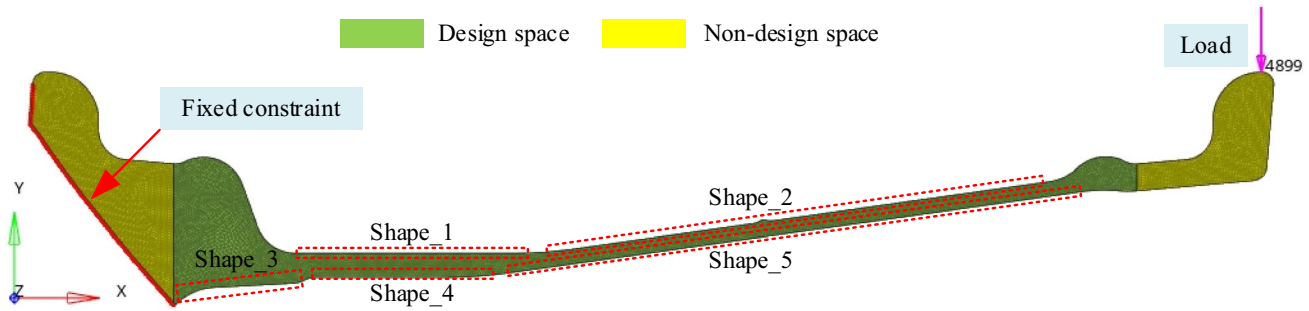

Fig. 12. Definition of design space and non-design space.

to discern principal contributing factors[36]. The procedural schematic of this DOE implementation is illustrated in Fig. 11.

Definition of shape variables

Firstly, the design and non-design spaces are defined in OptiStruct, as shown in Fig. 12. The material parameters of the rim (i.e., wheel) are given in Table 2. The element size is set to 0.5 mm to maintain the similarity between the discretised mesh model and the geometric model of the rim cross-section, and the element type is selected as shell elements with a thickness of 1 mm.

Subsequently, the load and boundary conditions are applied. Compared to the inner rim flange, the outer rim flange exhibits greater stiffness due to the support provided by spokes; thus, the fixed constraint is applied near the outer rim. Furthermore, the radial concentrated load F applied to the rim is set to 1 N, which is exerted to the node numbered 4899 (Node-4899), as shown in Fig. 12. To facilitate the subsequent discussion, the optimised areas of the rim are labelled, named shape_1, shape_2, shape_3, shape_4, and shape_5, respectively, while other areas remain unchanged due to considerations related to the tyre assembly. Specifically, the same structure (excluding shape_3) is divided into upper and lower parts when labelling the shape variables. Taking

Shape variable	Shape_1	Shape_2	Shape_3	Shape_4	Shape_5
Thinning value (mm)	0.5	0.5	1.5	0.5	0.5

Table 4. Maximum thinning value (mesh deformation) of each shape variable.

Shape variable	Shape_1 and Shape_2	Shape_3	Shape_4 and Shape_5
Range (mm)	− 0.5, − 0.25, 0, 0.25, 0.5	− 1.5, − 0.75, 0, 0.75, 1.5	− 0.5, − 0.25, 0, 0.25, 0.5

Table 5. Range of shape variables.

shape_2 and shape_5 as an example, the cutting amount of shape_2 and shape_5 may vary in actual production. Dividing the structure into shape_2 and shape_5 ensures their independence, thereby facilitating the search for an optimal solution.

Finally, the shape variables are defined. The optimisation requires reducing the rim thickness while ensuring the rim's strength, and achieving a lightweight rim. HyperWorks' mesh morphing technology implements shape variables, facilitating mesh deformation within distinct rim regions towards material reduction, where positive morphing coefficients correspond to thickness decrease. Considering potential reinforcement requirements in specific locations which necessitate sectional enlargement, the morphing coefficients' operational range is clamped at [− 1, 1]. In this convention, positive coefficient values induce localised thickness reduction within rim components, while negative values produce controlled thickening of critical zones.

The preceding analysis configures control handles at shape_1 through shape_5 to enable directional mesh morphing for rim thinning across distinct regions. The "Translate" deformation methodology is implemented when defining shape variables, permitting bidirectional deformation along the Y-axis. Considering actual product specifications and manufacturing constraints, shape_3 exhibits significantly greater material allowance than other regions. Consequently, enhanced mesh deformation parameters are explicitly applied to shape_3. Table 4 presents the maximum mesh deformation parameters per shape variable, corresponding to peak thinning values. This analysis deliberately excludes geometric parameters associated with transition zone corner radii when evaluating structural parameter influences on rim integrity. Subsequent engineering iterations will incorporate adjustments to corner radius parameters.

DOE analysis

The DOE methodology is applied to investigate the influence of rim structural parameters on mechanical stiffness and their mutual interactions. Within the DOE framework, the independent variables comprise five geometric descriptors of the rim structure (shape_1 to shape_5), while the output response corresponds to the maximum absolute radial displacement magnitude observed at Node-4899.

A simplified two-dimensional finite element model simulating the 90° impact scenario, developed within the OptiStruct environment, is subsequently imported into HyperStudy for parametric analysis. The OptiStruct solver is explicitly designated for computational execution. The mesh-deformation coefficients governing shape variation parameters are configured with discrete value constraints, implemented through a bounded parameter space ranging from − 1 to 1 with 0.5 interval increments, establishing the coefficient set {− 1, − 0.5, 0, 0.5, 1}. Shape variable quantification is subsequently derived through systematic interpolation between these discrete deformation coefficients and the prescribed maximum material thinning constraints.

$$shape\_i = t_i \times k, i \in \{1, 2, 3, 4, 5\} \tag{2}$$

where t_i is the maximum thinning value of shape_*i* (as shown in Table 4), and k is the mesh-deformation coefficient.

Taking shape_1 as an example, the maximum thinning value for shape_1 is t_1 = 0.5 mm. Consequently, based on Eq. (2), the range for shape_1 can be calculated as {− 0.5, − 0.25, 0, 0.25, 0.5} (units: mm). Similarly, the ranges for other shape variables can be determined, as presented in Table 5.

The DOE employs a full-factorial design approach[25]. This methodology encompasses all possible combinations of predefined factors, facilitating systematic examination of shape variable configurations across their respective value domains. Integration with HyperStudy's computational solver automates the evaluation of principal effects and factor interactions, enabling quantitative determination of parametric influences on rim structural integrity and cross-variable interdependencies.

Analysis results

The DOE analysis enables quantitative evaluation of each shape variable's effect on rim stiffness and their interactive relationships. As illustrated in Fig. 13, variable effects analysis demonstrates that shape_5 (42%) and shape_2 (39%) exhibit the most substantial percentage contributions to rim stiffness outcomes. Given the negative correlation between shape variables and local rim thickness, increased variable magnitudes correspond to wall thickness reduction, reducing rim stiffness and elevated deformation of the inner rim flange. The analytical findings support this mechanical response.

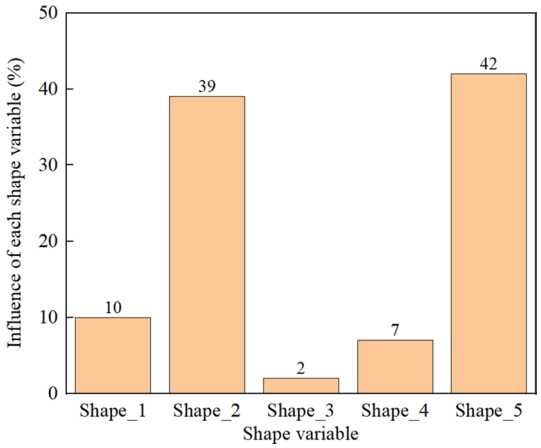

Fig. 13. The influences of shape variables on rim stiffness.

	Interaction effect				
Shape variable	**Shape_1**	**Shape_2**	**Shape_3**	**Shape_4**	**Shape_5**
Shape_1		0.11	0.09	0.60	0.34
Shape_2	0.11		− 1.79E-7	4.50E-3	5.05
Shape_3	0.09	− 1.79E-7		− 0.02	− 3.58E-7
Shape_4	0.60	4.50E-3	− 0.02		0.06
Shape_5	0.34	5.05	− 3.58E-7	0.06	

Table 6. The interaction effects among various shape variables.

The interaction effects among different shape variables are presented in Table 6. The positive values of the interaction effects indicate positive interactions among the variables, with larger values reflecting more significant interactions. The results indicate that the positive interaction effect between shape_2 and shape_5 is the greatest, while the negative interaction effect between shape_3 and shape_4 is the most significant. A comparison reveals that the positive interaction effect between shape_2 and shape_5 is significantly greater than the absolute value of the negative interaction effect between shape_3 and shape_4, indicating that shape_2 and shape_5 exert the most significant influence on rim strength. Therefore, when optimising the rim structure, priority should be given to shape_2 and shape_5.

The interaction effects between shape variables are presented in Table 6. Positive interaction effect coefficients indicate mutually reinforcing relationships between parameters, with larger absolute values denoting stronger interactions. Analysis reveals shape_2 and shape_5 exhibit the most substantial positive synergistic effect, while shape_3 and shape_4 demonstrate the most pronounced negative coupling effect. The comparative evaluation shows that the positive interaction magnitude between shape_2-shape_5 significantly exceeds the absolute value of shape_3-shape_4's negative interaction, establishing these two parameter pairs as the dominant contributors to rim structural performance.

The following conclusions can be drawn from the aforementioned DOE analysis results:

1. The stiffness of the rim is positively correlated with the thickness of different parts.
2. The effects of different shape variables on the rim stiffness are as follows: shape_2 and shape_5 exert the most significant influence, while shape_3 has the least. Consequently, the optimisation of the rim should prioritise reducing the thickness at shape_ 3.
3. The interaction effects among different shape variables indicate that the positive interaction effect between shape_2 and shape_5 is the greatest, while the negative interaction effect between shape_3 and shape_4 is the most significant.

Shape optimisation of rim structure

Based on these conclusions, the principal factors influencing rim stiffness are identified as critical parameters for structural optimisation. This study employs Shape_2 and Shape_5 as primary design variables for rim optimisation, implementing the optimisation strategy through the OptiStruct platform using the following methodology (as illustrated in Fig. 14):

The optimisation framework applies the Method of Feasible Directions (MFD)—a gradient-based optimisation algorithm that seeks optimal solutions by iteratively following feasible search directions within the constraint-admissible domain. Each feasible direction must satisfy two fundamental criteria: (1) constraint

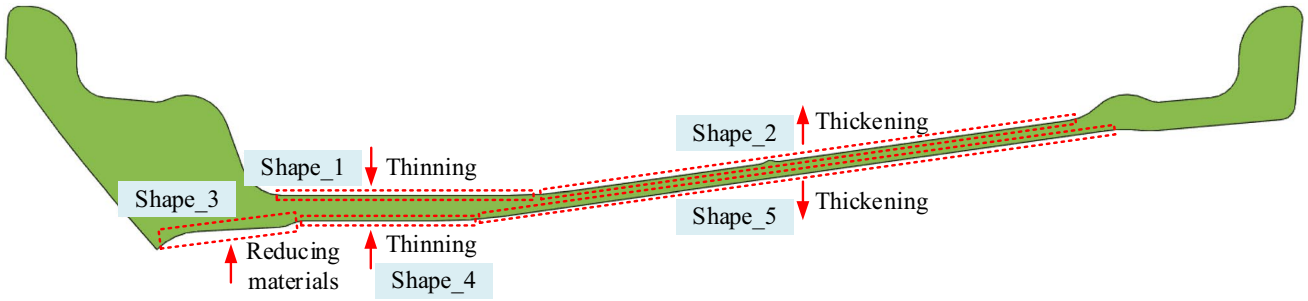

Fig. 14. Optimisation strategy for rim structure.

Shape variable	Shape_1	Shape_2	Shape_3	Shape_4	Shape_5
Sign of the coefficient	+	−	+	+	−

Table 7. The signs of the mesh deformation coefficients.

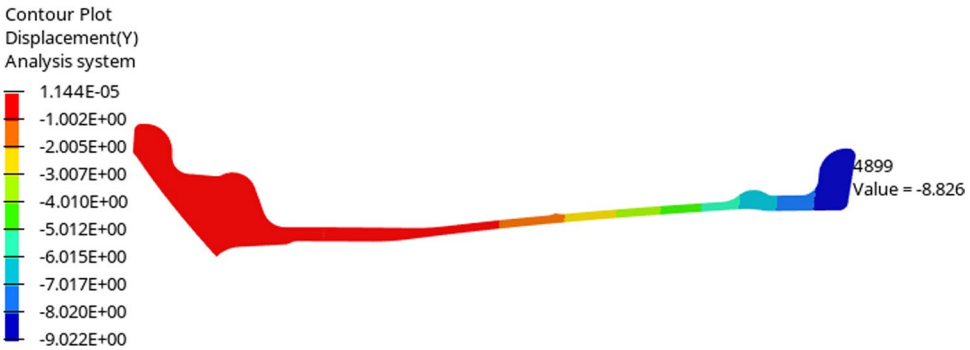

Fig. 15. The radial displacement of Node-4899 in the initial design.

feasibility through gradient projections and (2) objective function descent through directional derivative conditions.

Firstly, shape_2 and shape_5 will be optimised. Given that the stiffness of the rim is positively correlated with the thickness of different parts of the rim (Conclusion 1), and shape_2 and shape_5 have the most significant influence on the rim stiffness (Conclusion 2), along with the most significant positive interaction effect between shape_2 and shape_5 (Conclusion 3), both shape_2 and shape_5 will be thickened to enhance rim stiffness.

Subsequently, shape_1 and shape_4 will be optimised based on the information in Table 6. On one hand, in the interaction effects between shape_1 and shape_2, as well as between shape_1 and shape_5, the interaction effect between shape_1 and shape_5 is more significant and is positive. Since shape_5 has already been thickened, shape_1 must be thinned. On the other hand, in the interaction effects between shape_4 and shape_2, as well as between shape_4 and shape_5, the interaction effect between shape_4 and shape_5 is more significant and is positive; therefore, to enhance rim stiffness, shape_4 must be thinned.

Finally, shape_3 will be optimised. According to Conclusion 2, since shape_3 has a minimal effect on rim stiffness, most material will be removed from this area.

Given that the results of shape optimisation are manifested through mesh-deformation coefficients, the validity of the optimisation strategy can be corroborated by analysing the sign conventions of these coefficients. As expounded in Sect. "Definition of shape variables", a positive mesh-deformation coefficient denotes local wall thickness reduction in the rim profile, whilst a negative coefficient signifies wall thickness augmentation. In accordance with the optimisation framework depicted in Fig. 14, the prescribed sign allocations for each shape variable's mesh-deformation coefficients are comprehensively delineated in Table 7.

Before shape optimisation implementation, initial design variables exhibit zero-initialised mesh-deformation coefficients. Finite element analysis records a baseline radial displacement of − 8.826 mm at Node-4899 in the pre-optimised configuration, with corresponding spatial displacement mapping illustrated in Fig. 15.

The shape optimisation of the rim incorporates shape_1, shape_2, shape_3, shape_4, and shape_5 as geometric design parameters, constrained by maintaining the radial displacement at Node-4899 within original specification limits, to achieve mass minimisation. This shape optimisation problem is mathematically formulated as follows:

Shape variable	Shape_1	Shape_2	Shape_3	Shape_4	Shape_5
Mesh-deformation coefficient	0.1924	− 0.1182	1	0.68	− 0.2857
Thinning value (mm)	0.0962	− 0.0591	1.5	0.34	− 0.14285

Table 8. Results of shape optimisation.

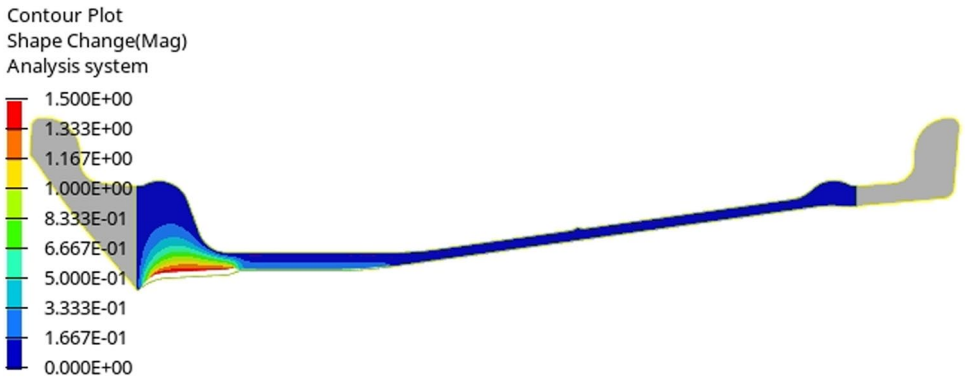

Fig. 16. The result of shape optimisation.

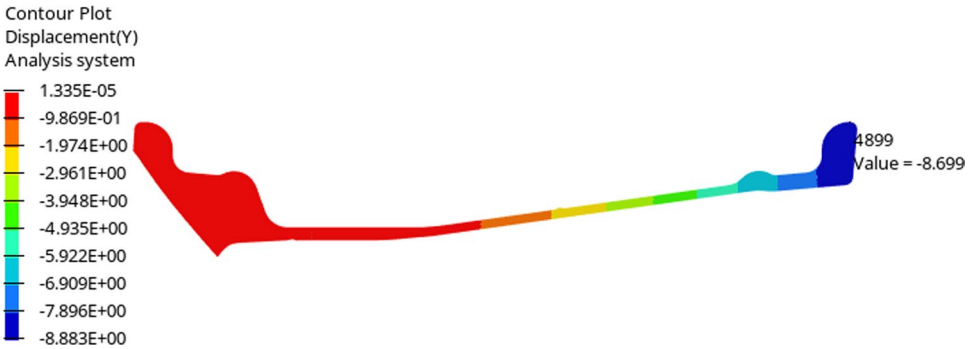

Fig. 17. The radial displacement of Node-4899 in the optimised design.

$$\begin{cases} \text{find } k, k \in [-1, 1] \\ Shape\_i = k \cdot t_i, i \in \{1, 2, 3, 4, 5\} \\ \text{s.t } D \leq D_0 \\ f(s) = \min M \end{cases} \tag{3}$$

where k is the mesh-deformation coefficient, t_i is the maximum thinning value of shape_i, D is the radial displacement of Node-4899 in the optimisation process, D_0 is the radial displacement of Node-4899 in the initial design, M is the mass of the rim.

The optimisation results are presented in Table 8, where negative values indicate local thickening of the rim. The signs of the mesh-deformation coefficients for shape_1, shape_2, shape_3, shape_4, and shape_5 are "+", "-", "+", "+", and "-", respectively, corresponding to those in Table 7, thus verifying the validity of the optimisation strategy.

The optimised rim profile is depicted in Fig. 16, with the associated deformation characteristics of Node-4899 illustrated in Fig. 17. Comparative analysis with the initial design (Fig. 15) reveals a 0.127 mm reduction in radial displacement at Node-4899, from 8.826 to 8.699 mm. This deformation reduction demonstrates enhanced bending resistance in the two-dimensional rim cross-section.

The results of the shape optimisation further indicate that:

1. The negative values for shape_2 and shape_5 indicate that thickening is required at these areas. Under the condition of the same value of the maximum mesh deformation, the mesh-deformation coefficient of shape_5 is 2.4 times that of shape_2, indicating that the thickening of shape_5 is 2.4 times greater than that of shape_2, which demonstrates that shape_5 withstands a more significant load.

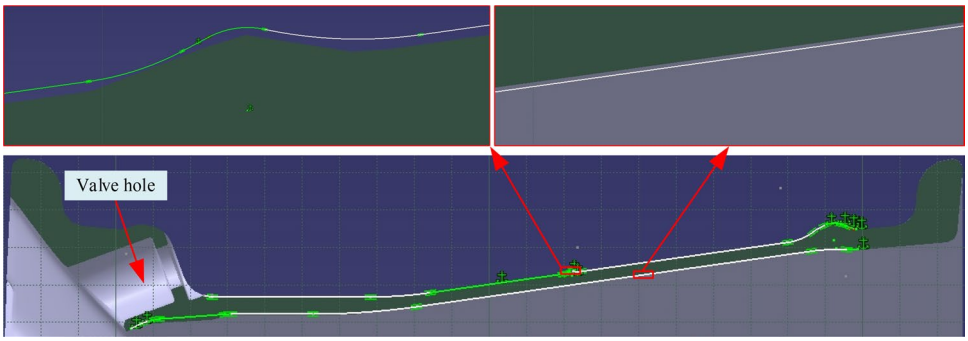

Fig. 18. The result of engineering modifications.

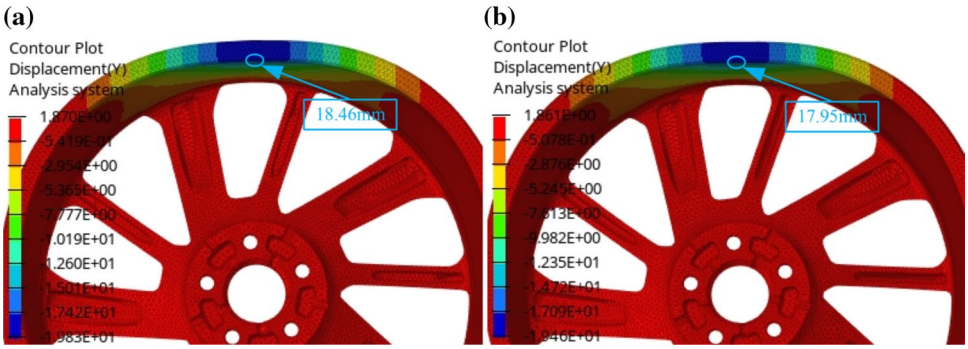

Fig. 19.. The radial deformation of the inner rim flange before and after optimisation. (**a**) Before optimisation, (**b**) After optimisation.

2. The positive values for shape_1 and shape_4 indicate that some material can be removed from these areas. Under the condition of the same value of the maximum mesh deformation, the mesh-deformation coefficient of shape_4 is 3.5 times that of shape_1, indicating that the thinning of shape_4 is 3.5 times greater than that of shape_1, which demonstrates that shape_1 withstands a more significant load.

Consequently, based on the shape optimisation results, for similar rim structures in the future, materials should primarily be distributed along shape_5. Conversely, a certain amount of material may be removed from shape_3 and shape_4 to reduce weight while maximising load-bearing capacity.

Verification of the optimisation with 3D simulation

Engineering modifications of the optimised rim

The baseline rim configuration underwent systematic replacement with the optimised geometry through Catia's "Surface Stitching" module, accompanied by precision engineering adjustments. These modifications comprised wall thickness modulation, elimination of sharp geometric discontinuities, and transitional curvature radii parameterisation. Post-optimisation mass analysis (Fig. 18) quantifies a 59 g mass reduction versus initial specifications.

Verification of rim strength

Optimisation based on 2D simplified models needs to be verified by a posteriori 3D simulation and experimental testing to verify its reliability. The limitations are mainly reflected in the simplified assumptions of 3D dynamic effects and load paths. The actual results may differ from the full model in local stress and energy distribution, but reasonable simplification can significantly improve efficiency.

A three-dimensional finite element model was constructed based on the optimised rim cross-section configuration, employing a hammer fall height of 228 mm with other parameters maintained at original specifications. The resultant simulation data, presented in the simulation results shown in Fig. 19, revealed a measured radial deformation of 17.95 mm at the inner rim flange in the optimised design. This demonstrates a 0.51 mm reduction in plastic deformation compared to the 18.46 mm displacement observed in the initial configuration. The optimised rim achieves both mass reduction and improved structural integrity, thereby confirming the efficacy of the shape optimisation methodology.

Conclusions

The 90° impact validation study and computational modelling were performed on a production 20 × 9.0 J aluminium alloy wheel. The experimental-simulation correlation demonstrated minimal relative error ($\delta < 5.04\%$), verifying the predictive accuracy of the finite element analysis framework for 90° impact scenarios and providing a validated foundation for subsequent rim structural optimisation.

The influence of multiple rim structural parameters on mechanical performance and their interaction effects was thoroughly examined through the design of experiments (DOE) analysis. Results demonstrated that geometrical parameters shape_2 and shape_5 exhibited the most significant impact on structural integrity, with their interaction showing statistical significance. Shape_3 demonstrated the least observable impact on load-bearing capacity, establishing this area as the optimal target for mass reduction in weight optimisation programmes.

Following design of experiments analysis, the rim underwent systematic shape optimisation. Engineering modifications were implemented on the baseline rim configuration, with subsequent finite element analysis verifying the optimised structure's mechanical integrity. Analytical results demonstrated a 0.51 mm reduction in radial deformation at the inner rim flange interface. This optimised geometric configuration achieved enhanced structural performance while achieving a mass reduction of 59 g through material redistribution strategies.

Through systematic analysis of parametric effects on rim structural integrity and their synergistic interactions, targeted implementation of mass optimisation strategies becomes feasible, consequently enhancing R&D operational efficiency in wheel system development.

Data availability

The datasets analysed during the current study are available from the corresponding author on reasonable request.

Received: 16 January 2025; Accepted: 17 June 2025
Published online: 09 July 2025

References

1. Teixeira, D. et al. Influence of injection molding on the flexural strength and surface quality of long glass fiber-reinforced polyamide 6.6 composites. *Mater. Des.* **85**, 695–706 (2015).
2. Miller, W. S. et al. Recent development in aluminium alloy for the automotive industry. *Mater. Sci. Eng.* **280**(01), 37–49 (2000).
3. Korkut, T. B. et al. Design and comparative strength analysis of wheel rims of a lightweight electric vehicle using Al6063 T6 and Al5083 aluminium alloys. *J. Achiev. Mater. Manuf. Eng.* **99**(02), 57–63 (2020).
4. Chai, W. H. et al. Research on simulation of the bending fatigue test of automotive wheel made of long glass fiber reinforced thermoplastic considering anisotropic property. *Adv. Eng. Softw.* **116**, 1–8 (2018).
5. Hu, D. Y. et al. Research on simulation method of impact resistance of composite wheels made of long glass fiber reinforced thermoplastic introducing anisotropic property. *Compos. Struct.* **223**, 110965 (2019).
6. Wang, D. F. & Xu, W. C. Fatigue failure analysis and multi-objective optimisation for the hybrid (bolted/bonded) connection of magnesium-aluminium alloy assembled wheel. *Eng. Fail. Anal.* **112**, 1–17 (2020).
7. Wang, D. F. et al. Design and optimisation of tapered carbon-fiber-reinforced polymer rim for carbon/aluminium assembled wheel. *Polym. Compos.* **42**(01), 253–270 (2021).
8. Wang, D. F. et al. Optimisation design of assembled wheel based on performance of fatigue and 13° impact. *J. Jilin Univ. (Eng. Edit.)* **48**(01), 44–56 (2018).
9. Wang, D. F., Zhang, S. & Xu, W. C. Multi-objective optimisation design of wheel based on the performance of 13° and 90° impact tests. *Int. J. Crashworthiness* **24**(03), 336–361 (2019).
10. Xu, W. C. & Wang, D. F. Influence study of connecting methods on the 90° impact performance of magnesium/aluminium assembled wheel. *Int. J. Adhes. Adhes.* **124**, 1–13 (2023).
11. ZH Wang. Research on key technology of lightweight design for aluminium alloy wheel hub. Dissertation, Yanshan University (2021).
12. YM Yang. Magnesium industry continues to pursue green development in 2021. China Nonferrous Metals News, 07 (2022).
13. Zhang, K. et al. Application research progress of CFRP in automobile lightweight. *Eng. Plast. Appl.* **50**(10), 154 (2022).
14. Tarang, S. et al. Fatigue analysis of alloy wheel using cornering fatigue test and its weight optimisation. *Mater. Today: Proc.* **62**, 1470–1474 (2022).
15. Yao, S. The use of aluminium alloys in structures: review and outlook. *Structures* **57**, 105290 (2023).
16. Lei, F. et al. An integrated optimisation for laminate design and manufacturing of a CFRP wheel hub based on structural performance. *Struct. Multidiscip. Optim.* **57**(06), 2309–2321 (2018).
17. Zhang, Y. et al. An integrated multi-objective topology optimisation method for automobile wheels made of lightweight materials. *Struct. Multidiscip. Optim.* **64**, 1585–1605 (2021).
18. Jiménez-Armendáriz, J. et al. Energy dissipation enhancement of thin-walled 6063 T5 aluminium tubes by combining a triggering mechanism and heat treatment. *Metals* **13**(05), 922 (2023).
19. Automobile Industry Standards of the People's Republic of China. QC/T 991-2015, 90 degree impact test method for light alloy wheels of passenger cars. Standards Press of China, Beijing (2015).
20. Zhao, L. H. & Bi, T. Fracture analysis and structure optimisation of low pressure casting aluminium rim. *Spec. Cast. Nonferrous Alloys* **42**(01), 119–121 (2022).
21. Pang, W. et al. Modeling and optimisation for lightweight design of aluminium alloy wheel hub. *Key Eng. Mater.* **723**, 322–328 (2016).
22. Zhang, Y. S. et al. Design of motorcycle aluminium alloy wheels. *J. Gansu Sci.* **26**(04), 123 (2014).
23. Suresh, B. K., Ramanaiah, N. & Ramamurty, R. P. Passenger cars wheel performance test simulation for service life evaluation: a review. *J. Fail. Anal. Prev.* **22**(04), 1370–1392 (2022).
24. Wang, D. F. et al. Topology optimisation and multi-objective optimisation of wheel based on fatigue tests. *Automot. Eng.* **39**(12), 1351 (2017).
25. Schäfer, C. & Finke, E. Shape optimisation by design of experiments and finite element methods-an application of steel wheels. *Struct. Multidiscip. Optim.* **36**, 477–491 (2008).
26. Hu, J. H. et al. Development and application of lightweight design of the aluminium alloy wheel. *Appl. Mech. Mater.* **310**, 253–257 (2013).
27. HM Sun. Modal analysis and optimisation design of vehicle aluminium alloy wheel. Dissertation, Yanshan University 2007.

28. Wang, H. Y. Geometric parameters optimal design of variable cross-section rim. *Proc. FISITA 2012 World Automot. Congress* **8**, 1003–1008 (2013).
29. Wang, Z. H. et al. Shape optimisation method for wheel rim of automobile wheels based on load path analysis. *Proc. Inst. Mech. Eng. Part C J. Mech. Eng. Sci.* **237**(02), 267–280 (2023).
30. Yang, G., Gong, J. & Huang, G. P. Crack analysis and structural optimisation of aluminium alloy wheel of new energy vehicle. *Intern. Combust. Engine Parts* **19**, 24–26 (2022).
31. Ballo, F. et al. Impact tests of wheels of road vehicles: A comprehensive method for numerical simulation. *Int. J. Impact Eng.* **146**, 103719 (2020).
32. Previati, G. et al. Radial impact test of aluminum wheels-numerical simulation and experimental validation. *Int. J. Impact Eng.* **126**, 117–134 (2019).
33. Zhang, G. D. et al. Numerical simulation on 90° impact test of aluminium alloy wheel with the effect of tyre. *Sci. Rep.* **14**, 1–16 (2024).
34. Gao, Q. et al. 90-degree impact bench test and simulation analysis of automotive steel wheel. *Eng. Fail. Anal.* **105**, 143–155 (2019).
35. YY Yu. Research on simulation of impact characteristics of motorcycle wheel. Dissertation, Chongqing University 2019.
36. Fang, X. J., Xu, Z. L. & Xiong, C. M. *OptiStruct and HyperStudy Optimisation and Engineering Applications* (China Machine Press, Monograph, 2023).

Author Contributions
All authors contributed to the study's conception and design. Shike Tao, Yangyang Zhou, ZhenYe, Jianjun Lu, Risheng Li and Shihui Li performed material preparation, data collection and analysis. Guangdong Zhang and Shike Tao wrote the first draft of the manuscript, and all authors commented on previous versions. All authors read and approved the final manuscript.

Funding
This work is supported by the Hebei Province Innovation Capacity Improvement Plan Project (Grant No. 24431003D) and the Baoding Science and Technology Plan Project (Grant No.2494C007)

Declarations

Competing Interests
The authors declare no competing interests.

Additional information
Correspondence and requests for materials should be addressed to G.Z.

Reprints and permissions information is available at www.nature.com/reprints.

Open Access This article is licensed under a Creative Commons Attribution-NonCommercial-NoDerivatives 4.0 International License, which permits any non-commercial use, sharing, distribution and reproduction in any medium or format, as long as you give appropriate credit to the original author(s) and the source, provide a link to the Creative Commons licence, and indicate if you modified the licensed material. You do not have permission under this licence to share adapted material derived from this article or parts of it. The images or other third party material in this article are included in the article's Creative Commons licence, unless indicated otherwise in a credit line to the material. If material is not included in the article's Creative Commons licence and your intended use is not permitted by statutory regulation or exceeds the permitted use, you will need to obtain permission directly from the copyright holder. To view a copy of this licence, visit http://creativecommons.org/licenses/by-nc-nd/4.0/.

© The Author(s) 2025